Article

Intercellular Stress Reconstitution from Traction Force Data

Juliane Zimmermann,[1,*] Ryan L. Hayes,[1] Markus Basan,[2] José N. Onuchic,[1] Wouter-Jan Rappel,[2] and Herbert Levine[1]

[1]Center for Theoretical Biological Physics, Rice University, Houston, Texas; and [2]Department of Physics and Center for Theoretical Biological Physics, University of California at San Diego, La Jolla, California

ABSTRACT Cells migrate collectively during development, wound healing, and cancer metastasis. Recently, a method has been developed to recover intercellular stress in monolayers from measured traction forces upon the substrate. To calculate stress maps in two dimensions, the cell sheet was assumed to behave like an elastic material, and it remains unclear to what extent this assumption is valid. In this study, we simulate our recently developed model for collective cell migration, and compute intercellular stress maps using the method employed in the experiments. We also compute these maps using a method that does not depend on the traction forces or material properties. The two independently obtained stress patterns agree well for the parameters we have probed and provide a verification of the validity of the experimental method.

INTRODUCTION

The collective migration of groups of cells is important in many biological processes, including development, wound healing, and cancer metastasis (1,2). Despite numerous experimental and theoretical studies, many aspects of collective migration are poorly understood. For example, it was generally believed that cells at the edge of monolayers move actively whereas cells in the bulk are dragged along passively (1). In support of this, the leader cells at the tips of fingerlike protrusions in wound-healing assays show a distinct morphology (3), and inclusion of leader cells into simulations predicts finger formation (4). However, recent studies showed that all cells, those in the bulk as well as those at the edge, contribute to motility by extending cryptic lamellipodia (5) and exerting forces on the substrate (6). As a consequence, stress builds up within the tissue. Some features of this stress can be understood using analytical models of the cell layer as an elastic sheet (7,8), but the overall interplay among contractile forces, cell-cell adhesion, and active traction forces remains poorly understood.

It is also still unclear how cells moving in a group align their motion. One possibility is that cells, in addition to responding to an external chemoattractant (9) and exchanging signaling molecules (10), interact via mechanical cues. Such a mechanism was incorporated into our recent model for collective cell migration. This model assumes that cells tend to align the direction of their motility force with their velocity, and showed that such a simple mechanism can lead to large-scale velocity correlations (11). Several experimentally observed phenomena, including swirling motion of cells in the tissue, buildup of tensile stress throughout the tissue, and finger formation at the edge (3), can be explained by this model (11). Another possibility is that cells align their motility according to the maximum principle direction of intercellular stress (6,12,13). Experiments showing that lamellipodia can develop in response to cell stretching, support such a mechanism (14).

Unfortunately, unlike the recovery of the average normal stress in a growing cell colony in one dimension that is based on a simple force balance (6), stress on cell-cell junctions cannot be directly measured in experiments. However, in 2011 Tambe et al. (13) developed a method to recover intercellular stress from measured traction forces on the substrate. The calculated stress maps in two dimensions required assumptions on the mechanical properties of the tissue. Specifically, the method solves elastic equations to recover two-dimensional stress maps from traction forces (13,15). Tambe et al. show that their method is not very sensitive to boundary conditions and the choice of a material property (the Poisson ratio) (15). However, their analysis, even with varying Poisson ratio, assumes that the cell layer is an elastic material, and it remains unclear whether the actual tissue, with cells dividing and moving actively, can in fact be described in this manner, or if a description as a fluid or viscoelastic material would be more appropriate. And, how do errors in tissue rheology translate to errors in the stress reconstruction?

Unlike in the experiments, simulations can provide both traction forces on the substrate and forces acting between cells. Therefore, we apply two different methods to calculate the intercellular stress using our recently developed collective cell migration model (11). This model has already been shown to reproduce basic features of the experimental data, and hence provides an excellent opportunity for understanding the validity of the traction-force based

Submitted November 25, 2013, and accepted for publication June 24, 2014.

*Correspondence: juliane@rice.edu

Editor: Margaret Gardel.

0006-3495/14/08/0548/7 $2.00

http://dx.doi.org/10.1016/j.bpj.2014.06.036

reconstruction for the actual experimental data. We use the same method as Tambe et al. (13) to recover the stress from traction forces, and apply a method used in molecular dynamics simulations to calculate the stress from interparticle forces (16). As we will show, both methods yield comparable two-dimensional stress maps, providing an independent validation of the experimental method.

METHODS

In our model simulations (Basan et al. (11,17) and see the Supporting Material), every cell is represented by two particles. They repel each other with the force $\mathbf{F}_{\mathrm{exp}}$, and when the distance between the particles crosses a certain threshold, the cell can divide and two new particles are inserted. Particles of different cells repel each other at short distances due to volume exclusion, and attract at longer distances, mimicking cell-cell adhesion (represented by $\mathbf{F}_{\mathrm{rep/ad}}$). Friction between the particles of one cell and different cells is accounted for by dissipative forces $\mathbf{F}_{\mathrm{int}}$ and $\mathbf{F}_{\mathrm{df}}$, respectively. A noise term η ensures that the total momentum is conserved (18). Intercellular forces act within a distance R_{cc}. Cells can be in a motile or in a nonmotile state. The motility force $\mathbf{m}$ that cells exert in the motile state has a fixed magnitude m and its direction is chosen randomly upon transition from the nonmotile to the motile state. In the simulation, the motility forces align with the velocities because the transition rate back to the nonmotile state is chosen to be smaller if they are aligned. Cells are also subject to friction with the substrate with force $\mathbf{F}_{\mathrm{B}}$. The equation of motion for one particle then reads

$$\frac{d\mathbf{p}}{dt} = \mathbf{m} + \mathbf{F}_{\mathrm{B}} + \mathbf{F}_{\mathrm{exp}} + \mathbf{F}_{\mathrm{int}} + \sum_{r<R_{cc}} \left(\mathbf{F}_{\mathrm{rep/ad}} + \mathbf{F}_{\mathrm{df}} + \eta\right). \quad (1)$$

The motility and friction force are exerted on the substrate and generate the traction forces that are used to reconstitute the stress with the first method (traction force method). All other forces are interparticle forces, and are used to calculate the stress using the second method (Hardy stress method).

The traction force method is described in Tambe et al. (13,15). Force balance in the tissue implies

$$\begin{aligned} \frac{\partial \sigma_{xx}}{\partial x} + \frac{\partial \sigma_{xy}}{\partial y} &= T_x^*, \\ \frac{\partial \sigma_{xy}}{\partial x} + \frac{\partial \sigma_{yy}}{\partial y} &= T_y^*, \end{aligned} \quad (2)$$

where $\mathbf{T}^* = -\mathbf{T}/h = (m + \mathbf{F}_{\mathrm{B}})/h$ and h is the monolayer height. The traction forces generated with our simulation model (Fig. 1, *B* and *C*) are very heterogeneous, similar to measured traction maps (6,13,15). Because the expressions in Eq. 2 consist of only two equations for the three unknown components of the stress tensor σ, the stress-strain relation of an elastic material

$$\begin{pmatrix} \sigma_{xx} \\ \sigma_{yy} \\ \sigma_{xy} \end{pmatrix} = \frac{E}{1-\nu^2} \begin{pmatrix} 1 & \nu & 0 \\ \nu & 1 & 0 \\ 0 & 0 & \frac{1-\nu}{2} \end{pmatrix} \begin{pmatrix} \epsilon_{xx} \\ \epsilon_{yy} \\ \epsilon_{xy} \end{pmatrix} \quad (3)$$

is assumed, where E is the Young's modulus and ν the Poisson ratio. The stresses are calculated with finite element analysis (see, e.g., Liu and Quek (19)), which corresponds to minimizing an energy functional. We assume quadratic elements and determine the displacements u_j at the grid points by solving the system of linear equations $\tilde{\mathbf{K}}\tilde{\mathbf{U}} = \tilde{\mathbf{T}}$, where $\tilde{\mathbf{K}}$ is the global stiffness matrix, $\tilde{\mathbf{U}}$ is the displacement vector, and $\tilde{\mathbf{T}}$ is the vector of the traction forces at all grid points. The traction forces on the grid points are determined by averaging the traction forces of the particles within a circle of radius R_{trac}. The stress is calculated in the entire computational domain and afterwards set zero in the areas where no cells are present (and traction forces are zero). Boundary conditions are chosen as in Tambe et al. (13,15) (zero displacement in the direction normal to the boundary of the computational domain). We also implemented zero-stress boundary conditions by restricting the computational domain to the actual tissue and fixing the displacement of two points within the tissue (Fig. 3 *C*, and see Fig. S2 *C* in the Supporting Material). The stresses calculated with this method are independent of the choice of E, and varying the Poisson ratio ν between 0.2 and 0.5 has only negligible effects (see Fig. S2).

The second method was developed by Hardy to calculate stress in molecular dynamics simulations (16). This method is more rigorous than the traction force method because it does not rely on any assumptions about the tissue properties. The components of the stress tensor arising from interparticle forces are given by

$$\sigma_{\alpha\beta}(\mathbf{R}, t) = -\frac{1}{2} \sum_{ij} F_{\alpha}^{ij} r_{\beta}^{ij} B\left(\mathbf{r}^i, \mathbf{r}^j, \mathbf{R}\right). \quad (4)$$

The contribution to the system-averaged stress by particles i and j is given by the negative product of interparticle forces $\mathbf{F}^{ij}$ and distance vectors $\mathbf{r}^{ij} = \mathbf{r}^i - \mathbf{r}^j$, normalized by the system volume. In Eq. 4, the contributions of particles i and j to the system-averaged stress are weighted by the bond function B such that only particles near the point $\mathbf{R}$ contribute to the stress at $\mathbf{R}$. If the line connecting particles i and j is within a distance R_{hs} of $\mathbf{R}$, the weight must be

$$B\left(\mathbf{r}^i, \mathbf{r}^j, \mathbf{R}\right) = \int_0^1 d\lambda \Delta\left(\lambda \mathbf{r}^{ij} + \mathbf{r}^j - \mathbf{R}\right), \quad (5)$$

whereas the localization function may be chosen to be

$$\Delta(\mathbf{r}) = \frac{2}{\pi h R_{\mathrm{hs}}^2} \left(1 - \left(\frac{\mathbf{r}}{R_{\mathrm{hs}}}\right)^2\right) \quad \text{if} \quad r<R_{\mathrm{hs}}. \quad (6)$$

We have verified that our results are insensitive to the exact choice of the localization function. We have also verified that the kinetic stress, computed following the methodology of Hardy (16), is negligible in our simulations. Changing the distance R_{hs} may change the stress on small length scales but does not influence the global stress pattern (see Fig. S1). It should be chosen large enough to average over sufficiently many particles but small with respect to the system size.

RESULTS AND DISCUSSION

We performed our simulations using the parameter set of Basan et al. (11) (see also Table S1 in the Supporting Material). Cells were seeded in our computational domain, and allowed to divide. A snapshot of the simulation, for a colony size of $N = 14{,}094$, is shown in Fig. 1 *A*. We then calculated stress maps using the two different methods. Fig. 1, *D* and *E*, shows the average normal pressure, which equals $-(\sigma_{xx} + \sigma_{yy})/2$, at each point. Red represents negative values (i.e., tensile stress), and blue represents positive values (i.e., pressure). The maps of the maximum shear stress computed using the two different methods are displayed in Fig. 1, *F* and *G*. This shear stress was computed as $(\sigma_{\max} - \sigma_{\min})/2$, where

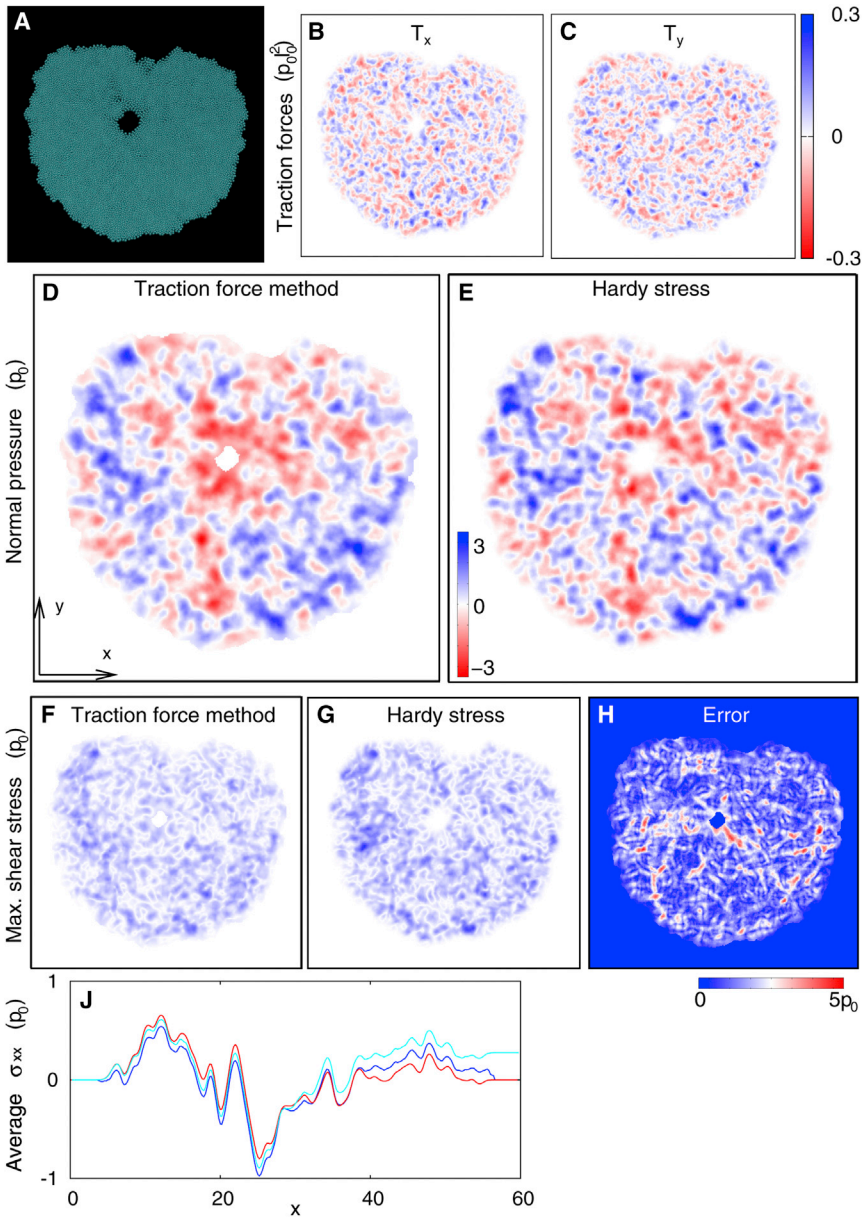

FIGURE 1 (*A*) Snapshot of the simulation with $N = 14{,}094$ particles. (*B* and *C*) The x and y component of the traction forces on the substrate in the simulation unit of force $p_0 l_0^2$. (*D* and *E*) Average normal stress and (*F* and *G*) maximum shear stress computed using simulation data. Panels *D* and *F* are calculated from traction forces upon the substrate whereas panels *E* and *G* are calculated from intercellular forces. Stresses are plotted using the indicated color scale: (*red*) tension, (*blue*) pressure; p_0 is the simulation unit of pressure. (*H*) Quantitative comparison (see text) between the components of the stress tensor computed with the two different methods using a color scale ranging from 0 (*blue*, maximal agreement) to 5 p_0 (*red*, minimal agreement). (*J*) Average of σ_{xx} along the y direction. (*Blue line*) Calculated from traction forces (map *D*). (*Red line*) Calculated from intercellular forces (map *E*). (*Cyan line*) Sum of the traction forces in the x direction averaged along the y direction (one-dimensional stress recovery method).

$\sigma_{\max}$ and $\sigma_{\min}$ are the maximum and minimum principal stresses.

A comparison between the maps reveals that the two methods produce qualitatively similar results. Notably, the location of prominent and large-scale areas of pressure and tension are identical whereas differences between the two maps can only be observed on small length scales. In addition, magnitudes of the large-scale patterns are comparable: the maximum values of normal stress differ by ~3% whereas the maximum values of shear stress differ by 20%. We can quantify the agreement between the stress maps by calculating the correlation as

$$c = \left(\sum \sigma_i^H \sigma_i^T\right)^2 \Big/ \left(\sum \sigma_i^{H^2} \sum \sigma_i^{T^2}\right),$$

where σ_i is the average normal pressure or the maximum shear stress at each point for the stress maps obtained using the traction force method (*T*) and the Hardy method (H), respectively. The comparison yields $c = 0.66$ for the pressure and $c = 0.79$ for the shear map. To further quantify the agreement between the stress tensors obtained with both methods, we computed for each point the absolute error

$$\epsilon = \left|\sigma_{xx}^T - \sigma_{xx}^H\right| + \left|\sigma_{yy}^T - \sigma_{yy}^H\right| + \left|\sigma_{xy}^T - \sigma_{xy}^H\right|.$$

The result is shown in Fig. 1 *H* using a color code with red corresponding to maximum values of ϵ and blue corresponding to minimal values of ϵ. Aside from a few areas with

small spatial scale discrepancies, the agreement between the two methods is quite satisfactory.

To gain further insight, we calculated the averaged one-dimensional stress profiles of the normal stress in the x direction. Fig. 1 *J* shows σ_{xx} averaged over the y direction for the traction force method (*blue curve*) and the Hardy method (*red curve*). We see that the pressure minimum is slightly lower for the traction stress but the differences are only marginal. We also calculated the sum of the average traction forces in x direction along this direction (*cyan curve* in Fig. 1 *J*), which corresponds to the one-dimensional stress recovery method reported in Trepat et al. (6) that does not require assumptions on material properties. The agreement with the two other methods is again very good. The sum of the traction forces in x direction (*cyan curve* in Fig. 1 *J*) does not exactly come back to zero, which indicates that there is a net force acting on the whole tissue (a similar effect was observed with the experimental data, see Trepat et al. (6). The total force fluctuates around zero due to the random choice of the direction of the motility force during transitions. However, we confirmed that the total force becomes zero when averaging over longer times (see Fig. S3). Deviations of the averaged net-traction force from zero are small because motility forces are largely balanced by friction forces, and align radially in circular spreading colonies.

The agreement between the two methods persists for a wide range of parameters. We have verified that increasing the division rate, the inclusion of a death rate into the model, and increasing the particle-particle adhesion do not significantly affect the agreement between the two methods. However, it does depend on having significant forces acting on the substrate. In Fig. 2, we show simulations with a different set of parameters, and explore the effect of decreasing the magnitude of the motility force on the substrate. The agreement becomes worse as the motility force decreases (Fig. 2 *G*). At first, the patterns still agree, but the traction-force method yields very weak magnitudes of stresses (Fig. 2, *C* and *D*). At very low motility forces (Fig. 2, *E* and *F*), the traction forces are almost zero and consequently stresses calculated with the traction force method are almost zero. However, the Hardy method still gives nonzero stresses. We thus conclude that stress patterns do not agree at very low traction forces, i.e., when stresses are dominantly created by intercellular forces. None of the experiments on actively growing tissues appear to reside in this range of force ratios, and hence the reconstructions from the experimental data should not be affected by this caveat.

As already mentioned, our model has been shown to reproduce many features of the tissue data. In particular, our model reproduces the heterogeneous traction force

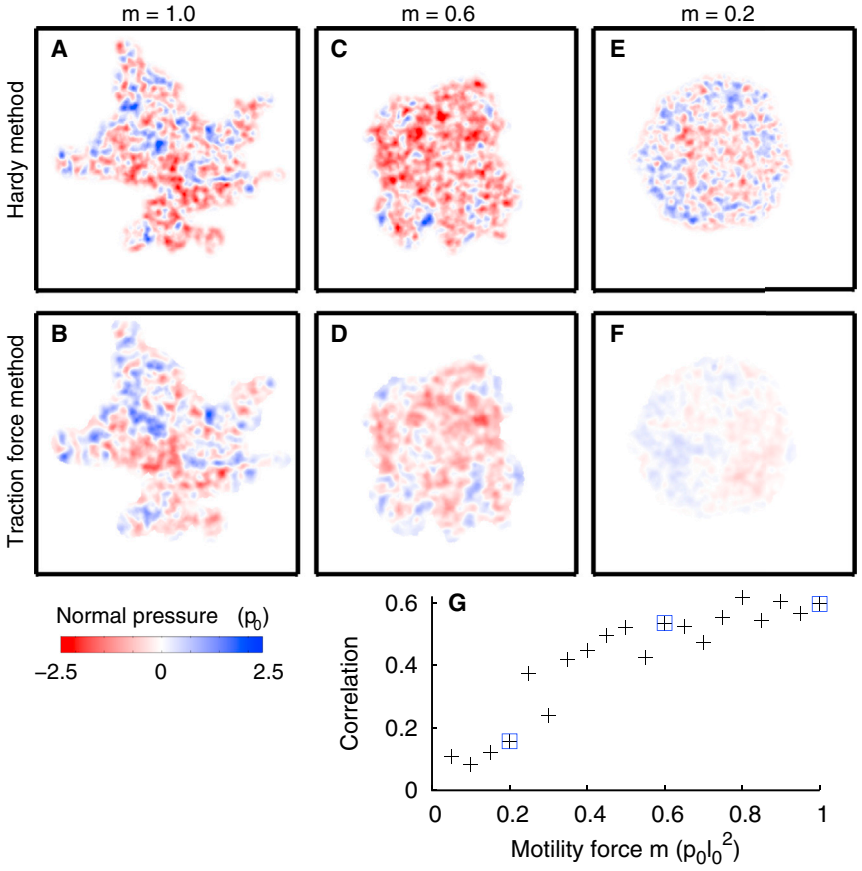

FIGURE 2 Maps of the average normal stress for different values of the magnitude of the motility force m. The agreement between both methods for stress calculation becomes worse as the strength of the motility force on the substrate decreases. Parameters with respect to the standard parameters used in Fig. 1: (*A* and *B*) Magnitude of the motility force $m = 0.83\ m^*$; transition rates to the nonmotile state $k^{\pm} = 0.1k^{\pm}{}^*$; transition rate to the motile state $k_{\text{wake}} = 0.025k^*{}_{\text{wake}}$; division rate $k_{\text{div}} = 0.5k^*{}_{\text{div}}$; and intercellular friction $\xi_{df} = 0.2\xi_{df}{}^*$. (*C* and *D*) Like panels *A* and *B*, but $m = 0.5\ m^*$. (*E* and *F*) Like panels *A* and *B*, but $m = 0.17\ m^*$. The values for m on the top are given in simulations units of the standard force $p_0 l_0{}^2$. (*G*) Correlation between stress tensors calculated with both methods $c = (\sum \sigma_{ij}^H \sigma_{ij}^T)^2 / (\sum \sigma_{ij}^{H2} \sum \sigma_{ij}^{T2})$, with the sum over all grid points $i = 1,\ldots,n$ and all components of the stress tensor at each grid point $j = xx,yy,xy$, for simulations with different values of m. (*Marked points*) Values for the maps shown above.

maps observed in large, motile tissues (6,13,15), and the stress maps generated with our simulation compare well with experimental results. In the model, motility forces align radially in spreading colonies because they tend to align with the velocities, and particles can only move away from the center. Tension builds up toward the center because opposing motility forces at opposite edges of the sheet pull on the adhering particles. Negative stress values (*red areas*) in Figs. 1 and 2 correspond to tensile stresses. In experimental studies, stresses were shown to be predominantly tensile and highest in the center of the tissue (6), or to be heterogeneous (but mostly tensile) (6,12). Both effects are observed with our simulation as well. Unlike in experiments, we do occasionally observe areas of high pressure, and a layer at the tissue edge where pressure is dominating due to cell division (Fig. 1 *J*). Small colonies are completely under tension whereas pressure builds up at the edge in larger colonies as the radial component of the locally averaged motility force reaches its maximum value (see also the discussion in Basan et al. (11)). It was also shown in experiments that the dominance of tension is dependent on cell-cell adhesion. Tension decreases upon application of a calcium chelator that disturbs contacts between neighboring cells (13). A similar effect is observed in our simulations (Fig. 3). In the simulation, decreasing cell-cell adhesion allows the two particles constituting a cell to move apart faster, which effectively increases the division rate, and leads to a dominance of pressure.

With pressure dominating in the stress maps (Fig. 3), normal stresses calculated with the traction force method (Fig. 3 *B*) are slightly shifted toward negative values due to the choice of boundary conditions. That is, because we assume zero displacement at the boundary of the quadratic domain, pressure in the center has to be compensated for by tension at the edge of the tissue. The agreement between the methods becomes better when choosing a zero-stress boundary condition at the tissue edge in the finite-element analysis instead (Fig. 3 *C*).

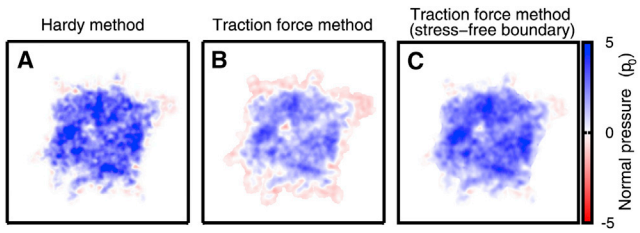

FIGURE 3 Average normal stresses are strongly dominated by pressure upon decreasing the cell-cell adhesion. Parameters are as in Fig. 2, *A* and *B*, but the strength of cell-cell adhesion is $f_1 = 0.9f_1^*$. (*A*) Stress calculated with the Hardy method. (*B*) Stress calculated from traction forces. Due to the choice of boundary conditions (zero displacement normal to boundary of quadratic domain), the traction force method does not capture the correct magnitude of stresses. (*C*) Stress calculated from traction forces with a zero-stress boundary condition at the tissue edge.

We should note that having vanishing traction forces on the substrate with vanishing motility forces (as in Fig. 2, *E* and *F*) might actually not be a biological relevant case. Cells in quiescent layers that are apparently nonmoving still exert large traction forces on the substrate. Measurements of traction forces exerted by groups of 2–30 MDCK cells or keratinocytes reveal that traction forces are largest at the outer boundary of the cell colonies (20–22). The distribution of traction forces in those cases is reminiscent of the force patterns observed with single cells (see, e.g., Wang et al. (23)), which supports the concept of the adhering cell cluster forming a supercell (24). Models describing the cell colonies as elastic sheets show that cell-cell adhesion and intracellular acto-myosin contraction are sufficient for generating the observed force pattern (7,8,20–22), and no explicit cell motility is required.

The tissues in the earlier-mentioned studies from Trepat et al. (6) and Tambe et al. (13,15) consist of >5000 cells (6). Those large sheets clearly rearrange due to cell division and collective migration. The traction forces in the substrate are still largest close to the edges but also measurable deep within the tissue. They are overall very heterogeneous, which has been attributed to the active motility of the cells. The seemingly different results for small nonmotile and large motile colonies could partly be explained by a difference in the strength of cell-cell adhesion. Mertz et al. (22) show that the predominant location of traction forces changes from the colony boundary to the sites of cell-cell contacts as the adhesion strength decreases.

Because cells are represented by only two particles in our simulation model, it obviously does not fully describe the traction force pattern of very small colonies, which is dominated by the force distribution of single cells. For sufficiently large colonies, we expect traction force patterns to become increasingly heterogeneous as the size of the colony grows (compare Fig. 3 *B*, in Basan et al. (11), and Fig. 1, *B* and *C*, here). Although exerting a motility force does not necessarily entail motion of a cell when it is balanced by motility forces from other adhering cells, alignment of traction forces with velocities promotes persistent motion of cells. Therefore, our model describes motile cells and is not suitable for quiescent cell layers. In order to encompass quiescent phenotypes, the model could be extended by a static term that leads to contractile substrate forces also in the limit of nonmoving cells.

In a recent experiment, Kim et al. (25) studied a sheet of cells migrating collectively toward a circular area of noncoated substrate. Cells can adhere and move everywhere except on this circular island. The tissue moves uniformly in one direction, splits in front of the island, and rejoins at the rear. Whereas traction forces and velocities are on average aligned in freely moving sheets, a surprising effect is observed at the boundary of the noncoated island: traction forces are always aligned perpendicular to the island boundary. It seems that cells permanently

try to invade the empty space. This behavior is particularly puzzling at the downstream stagnation point, where the tissue rejoins, because velocity and traction forces become uncoupled here, and point in opposite directions (25). Due to the alignment of the motility forces with the velocity in our model, we do not expect our simulation in the presented form to be able to reproduce those experimental findings. A static contraction of the sheet adhered to the substrate, or an active alignment of motility forces toward empty space, or some form of leader cells, need to be introduced in our model, and this is under investigation as of this writing. However, we are confident that those additional alignment effects of the motility forces do not affect the agreement between the two stress reconstitution methods.

CONCLUSION

We have compared stress maps obtained using a method suitable for experimental traction force microscopy versus those obtained by a method that directly computes the intercellular stress from the simulation data. Our results show that both methods produce qualitatively and quantitatively similar maps as long as traction forces are not too weak. Although in general the traction force method cannot resolve the full three-component stress tensor in the two-dimensional tissue, our work shows that nevertheless it provides a valuable estimation of local stresses within the tissue. The traction force estimation shows a remarkable agreement with the real stress field in a manner that appears to be relatively independent of tissue rheology in the model. A possible explanation for this agreement is the presence of low shear stresses. For zero shear stress, no stress-strain relation has to be assumed to solve the system in Eq. 2, and hence the reconstruction becomes exact. Shear stresses are typically low in our model because the interparticle forces are taken to be central forces. In addition, we make an assumption on the alignment mechanism of the motility force with the cell velocity. This mechanism is slightly different from the concept of plithotaxis, which has been previously proposed, and which assumes that the cellular motility aligns with the direction of principal stress in the tissue (12,13). Apparently, our alignment mechanism tends to create cells that move in clusters with little shearing between them. Although a model can never exactly describe the behavior of a real biological tissue, our assumptions yield tissue morphologies, flow fields (see Basan et al. (17)), and stress maps that agree well with experimental results. The success of our model and the demonstration here that traction-force-based reconstruction of intercellular stresses works well in the model gives us confidence that the same is in fact true for the data-based reconstruction, where obviously one cannot use the Hardy stress alternative to provide a direct confirmation.

SUPPORTING MATERIAL

Model description, results for varying parameters for stress computation, one table, and three figures are available at http://www.biophysj.org/biophysj/supplemental/S0006-3495(14)00680-8.

We thank Dr. Jeffrey Noel for helpful discussions.

This work was supported by National Science Foundation grant No. DMS-1068869 and by the National Science Foundation Center for Theoretical Biological Physics (grant No. NSF PHY-1308264). H.L. and J.N.O. were also supported by the Cancer Prevention & Research Institute of Texas Scholar program.

REFERENCES

1. Friedl, P., and D. Gilmour. 2009. Collective cell migration in morphogenesis, regeneration and cancer. *Nat. Rev. Mol. Cell Biol.* 10:445–457.
2. Rørth, P. 2012. Fellow travelers: emergent properties of collective cell migration. *EMBO Rep.* 13:984–991.
3. Poujade, M., E. Grasland-Mongrain, …, P. Silberzan. 2007. Collective migration of an epithelial monolayer in response to a model wound. *Proc. Natl. Acad. Sci. USA.* 104:15988–15993.
4. Sepúlveda, N., L. Petitjean, …, V. Hakim. 2013. Collective cell motion in an epithelial sheet can be quantitatively described by a stochastic interacting particle model. *PLOS Comput. Biol.* 9:e1002944.
5. Farooqui, R., and G. Fenteany. 2005. Multiple rows of cells behind an epithelial wound edge extend cryptic lamellipodia to collectively drive cell-sheet movement. *J. Cell Sci.* 118:51–63.
6. Trepat, X., M. R. Wasserman, …, J. J. Fredberg. 2009. Physical forces during collective cell migration. *Nat. Phys.* 5:426–430.
7. Edwards, C. M., and U. S. Schwarz. 2011. Force localization in contracting cell layers. *Phys. Rev. Lett.* 107:128101.
8. Banerjee, S., and M. C. Marchetti. 2012. Contractile stresses in cohesive cell layers on finite-thickness substrates. *Phys. Rev. Lett.* 109: 108101.
9. Zaritsky, A., S. Natan, …, I. Tsarfaty. 2012. Emergence of HGF/SF-induced coordinated cellular motility. *PLoS ONE.* 7:e44671.
10. Matsubayashi, Y., M. Ebisuya, …, E. Nishida. 2004. ERK activation propagates in epithelial cell sheets and regulates their migration during wound healing. *Curr. Biol.* 14:731–735.
11. Basan, M., J. Elgeti, …, H. Levine. 2013. Alignment of cellular motility forces with tissue flow as a mechanism for efficient wound healing. *Proc. Natl. Acad. Sci. USA.* 110:2452–2459.
12. Trepat, X., and J. J. Fredberg. 2011. Plithotaxis and emergent dynamics in collective cellular migration. *Trends Cell Biol.* 21:638–646.
13. Tambe, D. T., C. C. Hardin, …, X. Trepat. 2011. Collective cell guidance by cooperative intercellular forces. *Nat. Mater.* 10:469–475.
14. Weber, G. F., M. A. Bjerke, and D. W. DeSimone. 2012. A mechanoresponsive cadherin-keratin complex directs polarized protrusive behavior and collective cell migration. *Dev. Cell.* 22:104–115.
15. Tambe, D. T., U. Croutelle, …, J. J. Fredberg. 2013. Monolayer stress microscopy: limitations, artifacts, and accuracy of recovered intercellular stresses. *PLoS ONE.* 8:e55172.
16. Hardy, R. J. 1982. Formulas for determining local properties in molecular-dynamics simulations: shock waves. *J. Chem. Phys.* 76:622–628.
17. Basan, M., J. Prost, …, J. Elgeti. 2011. Dissipative particle dynamics simulations for biological tissues: rheology and competition. *Phys. Biol.* 8:026014.
18. Nikunen, P., M. Karttunen, and I. Vattulainen. 2003. How would you integrate the equations of motion in dissipative particle dynamics simulations? *Comput. Phys. Comm.* 153:407–423.
19. Liu, G. R., and S. S. Quek. 2003. The Finite Element Method: A Practical Course. Butterworth-Heinemann, Oxford, UK.

20. Saez, A., E. Anon, …, B. Ladoux. 2010. Traction forces exerted by epithelial cell sheets. *J. Phys. Condens. Matter.* 22:194119.

21. Mertz, A. F., S. Banerjee, …, E. R. Dufresne. 2012. Scaling of traction forces with the size of cohesive cell colonies. *Phys. Rev. Lett.* 108: 198101.

22. Mertz, A. F., Y. Che, …, V. Horsley. 2013. Cadherin-based intercellular adhesions organize epithelial cell-matrix traction forces. *Proc. Natl. Acad. Sci. USA.* 110:842–847.

23. Wang, H.-B., M. Dembo, …, Y. Wang. 2001. Focal adhesion kinase is involved in mechanosensing during fibroblast migration. *Proc. Natl. Acad. Sci. USA.* 98:11295–11300.

24. Khalil, A. A., and P. Friedl. 2010. Determinants of leader cells in collective cell migration. *Integr. Biol. (Camb).* 2:568–574.

25. Kim, J. H., X. Serra-Picamal, …, J. J. Fredberg. 2013. Propulsion and navigation within the advancing monolayer sheet. *Nat. Mater.* 12: 856–863.